



## UvA-DARE (Digital Academic Repository)

### Fluorescent molecular rotors

*From working principles to visualization of mechanical contacts*

Suhina, T.

#### Publication date

2017

#### Document Version

Other version

#### License

Other

[Link to publication](#)

#### Citation for published version (APA):

Suhina, T. (2017). *Fluorescent molecular rotors: From working principles to visualization of mechanical contacts*. [Thesis, fully internal, Universiteit van Amsterdam].

#### General rights

It is not permitted to download or to forward/distribute the text or part of it without the consent of the author(s) and/or copyright holder(s), other than for strictly personal, individual use, unless the work is under an open content license (like Creative Commons).

#### Disclaimer/Complaints regulations

If you believe that digital publication of certain material infringes any of your rights or (privacy) interests, please let the Library know, stating your reasons. In case of a legitimate complaint, the Library will make the material inaccessible and/or remove it from the website. Please Ask the Library: <https://uba.uva.nl/en/contact>, or a letter to: Library of the University of Amsterdam, Secretariat, Singel 425, 1012 WP Amsterdam, The Netherlands. You will be contacted as soon as possible.

## Solvent-polarity (In)dependent Deactivation of BODIPY Molecular Rotors\*

### Abstract

Molecular rotors based on *meso*-substituted boron-dipyrromethane (BODIPY) are widely recognized fluorescent viscosity sensors. The viscosity dependence of their fluorescence arises from an efficient excited-state deactivation process that can only occur when molecular-scale motion is not hindered. Here, we use visible and IR pump-probe spectroscopies combined with TD-DFT calculations to show that this fluorescence deactivation takes place through a fast and irreversible process which does not involve intermediate electronic states. Our data indicate that nonradiative excited-state deactivation of BODIPY molecular rotors is practically independent of solvent polarity, but strongly governed by viscoelastic/free volume properties of the local environment in both low- and high-viscosity regimes.

---

\* This chapter is adapted from:  
Suhina, T; Amirjalayer, S.; Woutersen, S.; Bonn, D.; Brouwer, A. M., *submitted*.

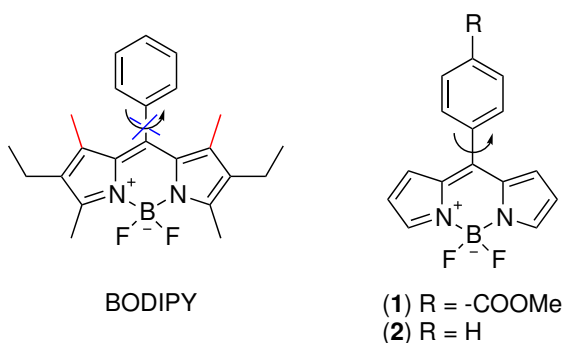
## 6.1 Introduction

Fluorescent molecular rotors provide the unique ability to probe the micro-viscosity of a molecular environment, and have thus found extensive use in biology, materials science and contact mechanics.<sup>1-16</sup> The dyes from the boron-dipyrromethene (BODIPY, see Scheme 6.1) family have attracted much attention since their initial discovery,<sup>17</sup> and their high level of customisability has made them popular in fluorescence labeling applications. BODIPY dyes were initially used due to their bright fluorescence and low-energy absorption which made them very useful markers for use in fluorescence microscopy. Upon removal of the substituents connected to the BODIPY core (indicated in red in Scheme. 6.1), however, fluorescence quantum yields greatly decrease.<sup>18</sup> This observation suggests that unhindered BODIPY derivatives behave like molecular rotors, and this idea has been further supported by calculations conducted on a semi-empirical level.<sup>18</sup>

Since the excited-state deactivation pathway requires significant changes in the geometry of the excited state, the viscosity of the environment has been found to govern the efficiency of fluorescence deactivation. This relation can be quantified by means of the widely-accepted Förster-Hoffmann relation:<sup>19,20</sup>

$$\ln(\Phi_f) = A + \alpha \ln(\eta), \quad (6.1)$$

where  $\Phi_f$  is the fluorescence quantum yield,  $\eta$  is the solvent viscosity, and  $A$  and  $\alpha$  are constants. For this reason, BODIPY derivatives similar to **1** (Scheme 6.1) have gained popularity as fluorescent probes for monitoring processes in which changes in micro-viscosity and/or free volume play an important role. Sol-to-gel transitions<sup>21</sup>, measurements of aerosol-particle,<sup>15</sup> intracellular,<sup>8,12</sup> or micro-bubble viscosities,<sup>11</sup> and monitoring phase separations in lipid membranes<sup>13</sup> are just a few examples where BODIPY rotors were used to monitor viscosity changes.



**Scheme 6.1:** Chemical structure of the structurally constrained BODIPY derivative (left) and the BODIPY derivative (right) studied in this work.

The large majority of experimental work on BODIPY-based molecular rotors is focused on viscoelastic environmental effects on their fluorescence prop-

erties.<sup>10–13,15,20–24</sup> Currently available information concerning the ultrafast and solvent dependent dynamics of these probes is limited.<sup>18,25,26</sup> In order to expand the understanding of the photo-physical behavior of these useful micro-viscosity probes, their excited-state deactivation must be examined as a function of both the viscoelastic and polarity response. Although the viscoelastic response has been studied in great detail,<sup>7,10,13,15,23</sup> energetic effects governed by the environment polarity and their influence on the excited-state deactivation of BODIPY rotors have, to our knowledge, not been studied. In this work, we aim to provide detailed photo-physical characterization of **1** on ultrafast time scales probed with transient visible (in non-polar toluene and polar MeCN) and mid-infrared absorption spectroscopy techniques (in polar MeCN) in order to obtain a detailed photo-physical picture of **1** and related BODIPY-based molecular rotors

## 6.2 Experimental

Compound **1** was prepared as reported in ref. 27. Solvents used in this work were of spectroscopic grade. Toluene and MeCN were additionally dried over 4 Å molecular sieves and passed through activated Al<sub>2</sub>O<sub>3</sub> before use. Experimental details of vis-pump/vis-probe and vis-pump/mid-IR probe can be found in Chapter 2 of this thesis.

### 6.2.1 Calculations

For DFT and TD-DFT calculations we used the Gaussian '09 software package.<sup>28</sup> All calculations were done either for isolated molecules ("vacuum") or with the PCM solvation model.<sup>29</sup>

## 6.3 Results and discussion

### 6.3.1 Steady state measurements

The absorption and emission spectra of **1** (see Fig. 6.1) exhibit mirror symmetry, indicating that the dominant bands originate from an S<sub>1</sub> ↔ S<sub>0</sub> transition. The spectral shapes and positions are very similar to those of BODIPY derivatives reported previously.<sup>18,25,26</sup> The Stokes shifts are small (< 1000 cm<sup>-1</sup>) and the spectra exhibit negative solvatochromism, which was previously observed for similar BODIPY derivatives<sup>7,25</sup> and suggests that dispersive interactions have a significant influence on the electronic spectra. Stokes shifts, although very small, slightly increase with solvent polarity and enable us to estimate the difference between the ground- and excited-state dipole moments to be ~ 1.4 D (see Appendix, Figs. 6.10 and 6.11). Although the fluorescence quantum yields reported for sterically unhindered BODIPY derivatives are generally low (~5-8 % in toluene<sup>7,8,18,26,30</sup>), the presence of the electron-withdrawing methyl ester group facilitates the fluorescence deactivation and results in Φ<sub>f</sub> values of ~0.8 % and ~0.5 % in toluene and

**Figure 6.1:** Normalized absorption (solid lines) and emission (dashed lines) steady-state spectra of **1** in MeCN and toluene.

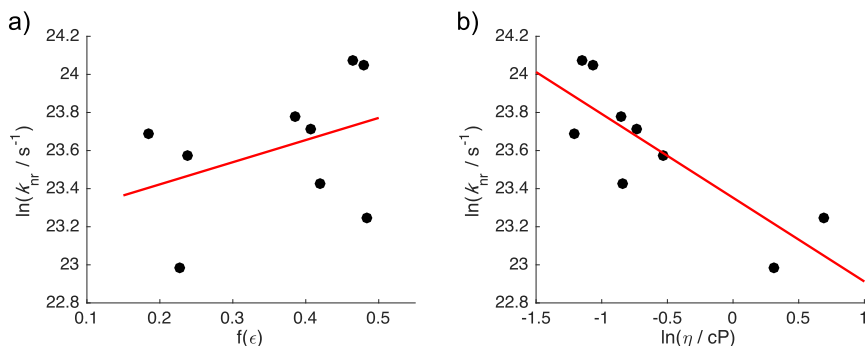
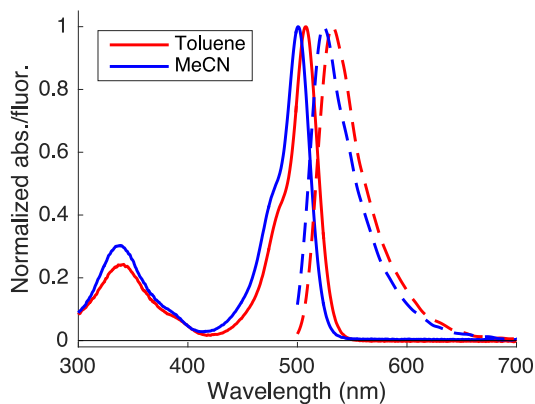


**Figure 6.2:** Linear correlation (red line) between a)  $\ln(k_{nr})$  and  $f(\epsilon)$ ; b)  $\ln(k_{nr})$  and  $\ln(\eta)$ . Only pure, low viscosity solvents were taken into account.

MeCN, respectively. These are, to our knowledge, the lowest  $\Phi_f$  values reported to date for this type of molecular rotors, and make this probe an excellent candidate for use in high-contrast imaging applications

In order to compare and quantify the influence of solvent polarity and viscosity on the excited-state deactivation rate, we measured fluorescence quantum yields of **1** in a set of low-viscosity aprotic solvents listed in Appendix Table 6.1. The nonradiative decay rate constant can be obtained from Eq. 6.2, where  $k_r$  is the radiative rate constant obtained from lifetime measurement of **1** in a confined medium in which the fluorescence deactivation is strongly suppressed (PMMA:  $\tau_{avg}=7.12$  ns; see Appendix, Fig. 6.12).

$$k_{nr} = k_{rad} \left( \frac{1}{\Phi_f} - 1 \right) \quad (6.2)$$

We interpret the obtained nonradiative rates in terms of hydrodynamic theory:

$$k_{nr}/T = C \eta^{-\alpha}, \quad (6.3)$$

where  $C$  represents the geometry dependent rotational friction coefficient of the particle and  $T$  represents the temperature. At constant temperature, this expression can be rearranged and becomes analogous to the expression derived by Förster and Hoffmann (Eq. 6.1). If an activation barrier is present, this expression needs to be modified to account for the response of the energy barrier towards changes in solvent polarity:<sup>9</sup>

$$k_{nr}/T = C \eta^{-\alpha} \exp\left(\frac{-E_a + p f(\epsilon)}{RT}\right), \quad (6.4)$$

where  $E_a$  represents the activation barrier of the excited-state deactivation process,  $p$  is a constant and  $R$  is the gas constant.  $f(\epsilon)$  represents the solvent's dielectric polarization function defined as  $f(\epsilon) = (\epsilon - 1)/(2\epsilon + 1)$ ,<sup>31</sup> where  $\epsilon$  is the relative permittivity of the solvent. According to Eq. 6.4,  $\ln(k_{nr})$  should show a linear dependence on  $f(\epsilon)$  and  $\ln(\eta)$ . Nonradiative rates as a function of solvent polarity and solvent viscosity are shown in Fig. 6.2 a) and b), respectively. While there is an obvious correlation between  $\ln(k_{nr})$  and  $\ln(\eta)$  (with slope  $\alpha$  of  $-0.44 \pm 0.3$  and  $R^2 = 0.63$ , Fig. 6.2 b)), the points in Fig. 6.2 a) are too scattered (slope =  $1.2 \pm 2.5$  and  $R^2 = 0.02$ ) to conclude whether  $\ln(k_{nr})$  shows dependence on solvent polarity. In order to assess the statistical significance of the correlations, we calculate the Pearson correlation coefficient<sup>32</sup> ( $r$ ) of  $\ln(k_{nr})$  vs  $\ln(\eta)$  and  $\ln(k_{nr})$  vs  $f(\epsilon)$ . The values of  $r$  can vary from -1 (anticorrelated) to 1 (strongly correlated), with the intermediate value of 0 when there is no correlation between the variables. The Pearson correlation coefficient obtained for  $\ln(\eta)$  vs  $\ln(k_{nr})$  points towards a significant level of (anti)correlation between  $\ln(\eta)$  and  $\ln(k_{nr})$  ( $r = -0.82$ , with probability of the two variables being uncorrelated  $p = 0.006$ ). The same can, however, not be claimed for  $f(\epsilon)$  and  $\ln(k_{nr})$  ( $r = 0.238$ ,  $p = 0.31$ ) at a significance level of 95 % (for which the limiting value of  $p = 0.05$ ). Based on this, we conclude that solvent viscosity plays a significant role in fluorescence deactivation of **1**, while the solvent polarity has only a minor (if any) influence on the nonradiative rates.

To examine the influence of solvent viscosity on nonradiative decay rates at higher viscosities, we measured fluorescence quantum yields of **1** in glycerol solutions at different temperatures between 290 and 320 K, and calculated the viscosity values according to ref. 33. If the hydrodynamic model holds,  $k_{nr}/T$  should be inversely proportional to the solvent viscosity ( $\alpha = 1$ ). A linear fit to the data shown in Fig. 6.3 yields a slope of  $-0.74$ , which demonstrates a high degree of correlation between the excited-state deactivation rate and the bulk viscosity of the solvent.

### 6.3.2 Sub-picosecond dynamics probed in the vis range

Transient absorption spectra of **1** in toluene and MeCN were measured by means of visible pump/visible probe spectroscopy. Representative transient spectra in Fig. 6.4 a) and c) with representative time traces in Fig. 6.4 b) and d) are shown for toluene and MeCN, respectively.

**Figure 6.3:** Nonradiative rates of **1** in glycerol measured as a function of temperature-regulated viscosity.

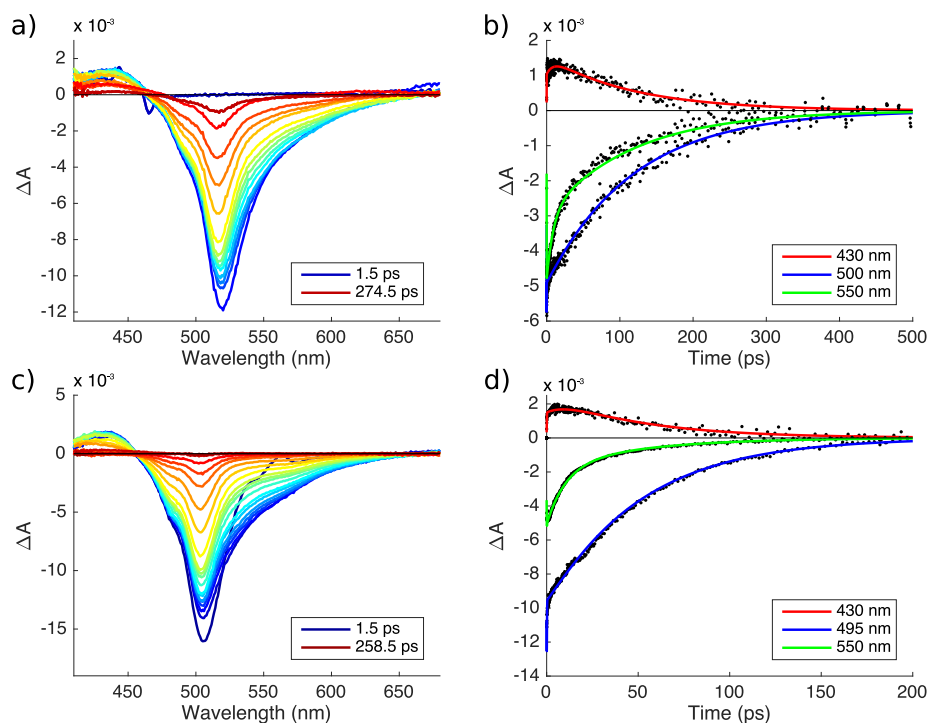
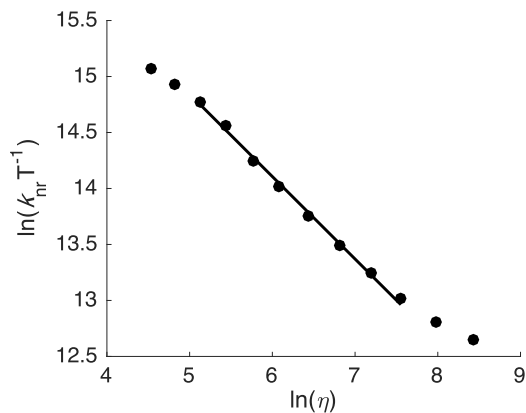
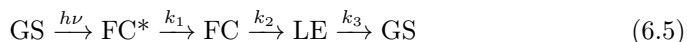


**Figure 6.4:** Representative transient spectra and time traces obtained by pump probe measurements (excitation at 488 nm) in the visible region: a) and b) toluene; c) and d) MeCN. Lines represent fits obtained by global analysis of the whole transient data matrix.

Since the solvent polarity does not have a significant impact on the spectral position and shape of the absorption and emission spectra, the two sets of transient spectra look very similar. Three distinguishable regions are observed. Excited-state absorption (ESA) occurs at relatively high energies ( $\sim 430$  nm) and overlaps partially with the ground-state bleach (GSB) which gives rise to the negative signal centered at  $\sim 500$  nm. Due to the small Stokes shifts, the ground-state bleach overlaps with the stimulated emission (SE) signal detectable in the 500-600 nm range. Global analysis of the whole transient data matrix, assuming a sum of exponential time profiles at each wavelength, produces time constants of  $\tau_1 = 1.08 \pm 0.01$  ps;  $\tau_2 = 11.92 \pm 0.09$  ps;  $\tau_3 = 114.76 \pm 0.17$  ps in toluene and  $\tau_1 = 0.65 \pm 0.01$  ps;  $\tau_2 = 9.40 \pm 0.04$  ps;  $\tau_3 = 49.90 \pm 0.06$  ps in MeCN. The reconstructed decay-associated difference spectra (DADS) of these components are shown in Fig. 6.5 a) and c) for toluene and MeCN, respectively. While the decay in MeCN is considerably faster, decay-associated difference spectra are very similar for both solvents. The decay of the ESA signal (positive amplitude) is associated with the longest time constant  $\tau_3$  in case of both solvents, while the observed rise in the ESA signal is associated mainly with  $\tau_2$  (negative amplitude). A small positive amplitude associated with this component can be observed in the GSB signal, indicating the possibility of vibrational cooling or formation of an excited-state species in this region. In SE, all three components are present. The shortest component ( $\tau_1$ ) is associated with positive amplitude, while the other two components ( $\tau_2$  and  $\tau_3$ ) are associated with negative amplitudes in the case of both solvents, which indicates that the species associated with time constants  $\tau_2$  and  $\tau_3$  are emissive.

In order to reconstruct spectra associated with the individual species, we model the kinetics using a global analysis of the transient data matrix by assuming a sequential scheme:



In this kinetic scheme, after vertical excitation ( $h\nu$ ) to the Franck-Condon region (FC), **1** relaxes in two fast steps via FC\* and FC to the locally excited state (LE). The first relaxation steps ( $k_1$  and  $k_2$ ) involve solvent and vibrational relaxation, but we also consider the possibility of a distinct structural difference between FC and LE, as discussed below. We assign this LE state to the relaxed excited-state, of which the geometry is obtained by the TD-DFT calculations presented below. After reaching the LE state, the molecule "diffuses" on the potential energy surface and this ultimately results in depopulation of the excited state ( $k_3$ ). Global analysis with this sequential model was performed on the whole transient-data matrix, and reconstructed species-associated difference spectra are shown in Fig. 6.5 b) and d) for toluene and MeCN, respectively. Representative time traces together with the results of the fits are shown in Figs. 6.4 b) and d) for **1** in toluene and MeCN, respectively. The shortest, ultrafast component is characterized by a rise of the red edge of the SE signal at very short delay times (see Appendix, Fig. 6.14 and DADS in Fig. 6.5 a) and c)) and does not exhibit significant contribution in the ESA region nor in transient IR measurements (see Fig. 6.5 a) and c), Appendix

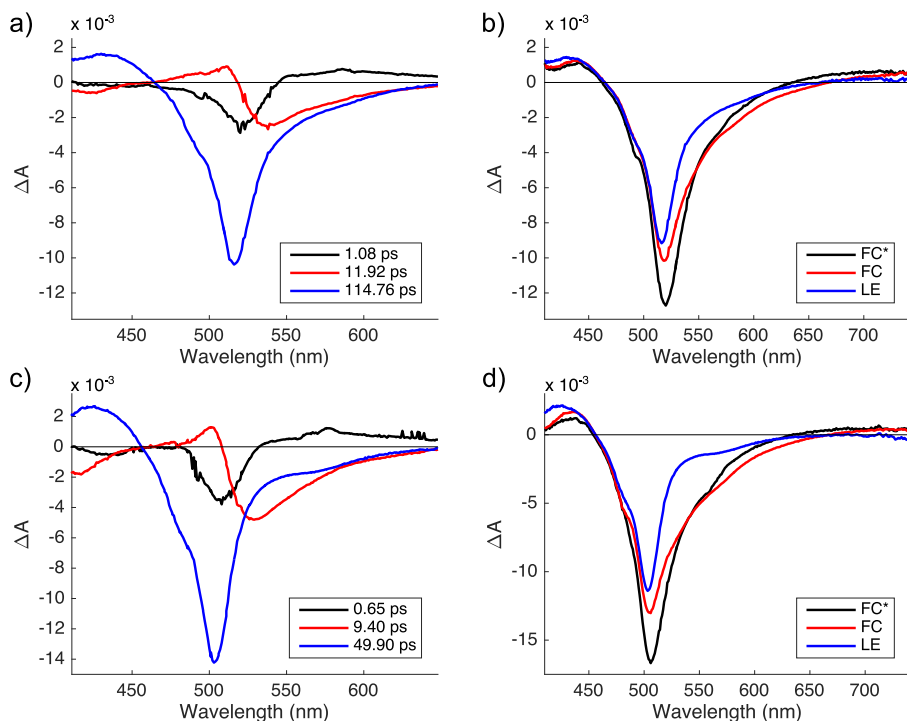


**Figure 6.5:** Decay and species associated spectra obtained in visible region for **1** in toluene and MeCN: a) and c) show decay associated difference spectra (with associated time constants) obtained in toluene and MeCN, respectively; b) and d) show species associated difference spectra for the sequential evolution (Eq. 6.5) obtained in toluene and MeCN, respectively.

Fig. 6.13, and IR measurements below). The time constants associated with this component ( $\tau_1$ ) obtained by fitting individual time traces obtained in the SE region become slower towards lower energies for **1** in both MeCN and toluene. Based on this observation, we attribute this time constant to the ultrafast solvation process. The second (fluorescent) component, on a ps time-scale, was previously reported for both unhindered and hindered BODIPY derivatives (see Fig. 6.1),<sup>18,25,26,30</sup> and has been attributed to vibrational relaxation<sup>25</sup> or conformational evolution associated with BODIPY-core structural changes in the excited state.<sup>26</sup> Although our vis-pump/vis-probe measurements clearly show this component, the analysis of vis-pump/vis-probe transient data indicates very small spectral changes (species spectra associated with the FC and LE components are located in similar spectral regions, Fig. 6.5 b) and d)), which could easily be attributed to either one of the previously proposed causes for this component. Additional data obtained by vis-pump/mid-IR probe measurements (see below), however, suggest formation of a distinct transient species associated with this ( $\tau_2$ ) time constant. The final, slowest time constant is attributed to the decay of the fully relaxed excited state and

shows excellent agreement with the values calculated from the intrinsic radiative lifetime of **1**, indicating structural similarity between this fluorescent component and the ground-state geometry.<sup>34</sup>

### 6.3.3 Picosecond dynamics probed in the mid-IR range

In order to obtain more information on the structural changes that take place in the excited state, we performed vis-pump/mid-IR probe experiments of **1** in MeCN. The FTIR spectrum is shown in 6.6 a), and representative transient spectra are shown in Fig. 6.6 b). The ground-state bleach band centered around  $1726\text{ cm}^{-1}$  corresponds to the C=O stretch mode of the methyl ester group. An excited-state absorption peak which we assign to vibrational modes located on the phenyl ring is found at  $\sim 1594\text{ cm}^{-1}$ . Two additional GSB bands are centered at  $\sim 1574\text{ cm}^{-1}$  and at  $\sim 1550\text{-}1560\text{ cm}^{-1}$ , and are attributed to vibrational modes of the BODIPY core and the phenyl ring (based on the frequencies obtained by TD-DFT). A broad excited-state absorption band centered around  $1519\text{ cm}^{-1}$  shows a rise and decay component (Fig. 6.6 b)) and suggests formation of a different transient species. TD-DFT calculations predict multiple vibrational modes in this region, which makes their direct assignment difficult. These modes, however, involve vibrations localized on the BODIPY core which are mixed with modes on the phenyl ring (see Fig. 6.15). A lower-energy ESA band is located at  $\sim 1495\text{ cm}^{-1}$  and is also attributed to vibrational modes on the core and the phenyl ring. The transient-data matrix was globally fitted using the sequential model ( $\text{FC} \xrightarrow{k_1} \text{LE} \xrightarrow{k_2} \text{GS}$ ), with time constants of  $\tau_1 = 10.8 \pm 0.1\text{ ps}$  and  $\tau_2 = 47.3 \pm 0.2\text{ ps}$  which are in excellent agreement with the values obtained from visible transients. The resulting species associated difference spectra are shown in Fig. 6.6 d). The reconstructed spectra show that the ESA of the FC state lacks the band centered at  $\sim 1519\text{ cm}^{-1}$  (or at least its amplitude appears to be smaller). Upon relaxation to the LE state, the band located at  $1519\text{ cm}^{-1}$  appears and the C=O stretch band shifts to slightly lower energies. The appearance of a new band at  $1519\text{ cm}^{-1}$  suggests that two components labeled FC and LE are different transient species and not only the result of vibrational cooling. The LE ESA spectrum (obtained by subtracting the scaled FTIR spectra from the LE SADS spectra) is compared to the calculated vibrational spectrum of CAM-B3LYP vacuum-optimized geometry of **1** in Fig. 6.6 e). While the TD-DFT calculation correctly predicts the shifts of the C=O stretch band, and the aromatic ring vibrations at  $1593\text{ cm}^{-1}$  and  $1499\text{ cm}^{-1}$ , the relative intensities are not well predicted, and the broad feature at  $1519\text{ cm}^{-1}$  remains unexplained.

### 6.3.4 DFT calculations

In order to get further insight into the excited-state dynamics of **1**, we performed geometry optimizations and frequency calculations at the TD CAM-B3LYP/6-31+G(d,p) level of theory,<sup>35</sup> which we chose based on its good performance in describing charge-transfer systems.<sup>35-38</sup> For the excited-state potential energy sur-

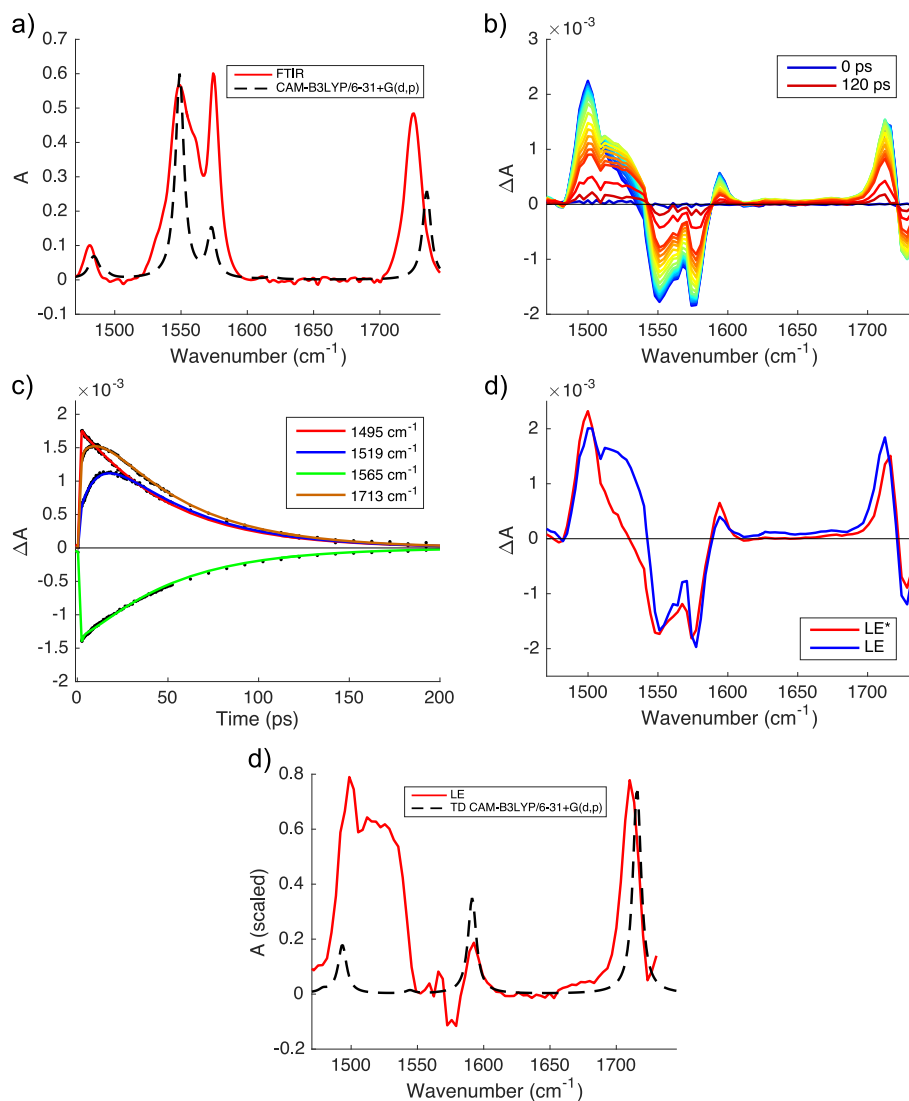


**Figure 6.6:** Infrared spectra of **1** in MeCN: a) Partial experimental (FTIR, red) and calculated (black, freq. scaled by 0.952) spectra of **1**; b) Vis pump/IR probe difference spectra at different time delays; c) time traces with fits; d) Species associated difference spectra obtained by global analysis with sequential model; e) Experimentally obtained LE spectrum and calculated spectrum (black, freq. scaled by 0.946).

face scans, after testing both basis sets, we opted for a simplification of the basis set to 6-31G(d), since we found it to be sufficient for describing the trends exhibited by **1** in its ground and excited states. In the main text we present an overview of the theoretical results, while a more detailed discussion and additional results can be found in the Appendix.

$S_0$  and  $S_1$  vacuum-optimized geometries are shown in Fig. 6.7. The lowest-energy excitation band corresponds mainly to the HOMO  $\rightarrow$  LUMO transition, with a small HOMO-1  $\rightarrow$  LUMO contribution. The electron density of the HOMO is located on the BODIPY core, but spreads over the phenyl ring in the LUMO, indicating some degree of charge-transfer character. The presence of LUMO electron density on the carbonyl group suggests that the electronic influence of the substituent may play a role in the deactivation process. The optimized ground-state structure is characterized by a planar BODIPY core geometry (Fig. 6.7 a) which forms a dihedral angle with the *meso*-phenyl ring of  $57.7^\circ$  (referred to as B-Phe dihedral throughout the rest of this chapter). The vacuum optimized excited-state structure is characterized by a reduced B-Phe dihedral value ( $47.3^\circ$ ), and a slight distortion of the boron atom out of the core plane (Fig. 6.7 b)). Including toluene or MeCN solvation results in B-Phe dihedral values similar to the ones obtained in vacuum, but the BODIPY core remains planar (Fig. 6.7 b)).

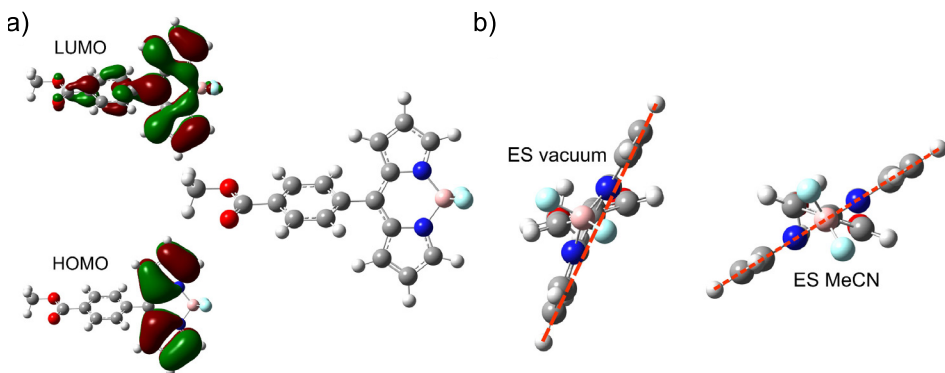


**Figure 6.7:** (TD) CAM-B3LYP/6-31+G(d,p) optimized geometries of **1**. a) Ground state with HOMO and LUMO frontier orbitals (vacuum); b) Locally excited-state structure obtained by optimization starting from the ground-state optimized geometries in vacuum and in MeCN.

The partially relaxed ground-state potential energy surface scan (Fig. 6.8 a)) reveals two local minima on the BODIPY ground-state potential energy surface separated by a small energy barrier of  $\sim 1$  kcal mol $^{-1}$ , which the molecules can easily overcome at room temperature. These two ground-state conformers are expected to interconvert rapidly. As the B-Phe dihedral nears  $0^\circ$  (or  $180^\circ$ ), the energy sharply rises. Changes in the B-Phe dihedral angle towards  $0^\circ$  (or  $180^\circ$ ) results in significant distortions of the BODIPY core, similar to the previously calculated structure by Alamiry *et al.*<sup>7</sup> The calculated dipole moment remains

practically unchanged (we obtained a decrease of  $\sim 0.7$  D) upon this motion and indicates that solvent polarity does not have a significant energetic effect on the ground-state energy surface.

An  $S_1$  excited-state potential energy surface scan ( $S_1$  optimized geometries with TD CAM-B3LYP/6-31G(d) in vacuum is shown in Fig. 6.8 b). The potential energy surface was obtained by fixing the B-Phe dihedral, while leaving the other coordinates to vary freely. Similarly to the ground-state scan, two minima (separated by an energy barrier of  $\sim 3.2$  kcal mol $^{-1}$ ) are found. These minima are attributed to the LE species observed in our transient measurements. The two additional, apparently global minima probably do not represent physically accessible minima as surface crossing seems to take place near B-Phe dihedral values of  $30^\circ$  and  $150^\circ$  (see below). Calculated dipole moments increase by  $\sim 3$  D as the B-Phe dihedral twists away from the optimized excited-state structures in case of **1**, but this difference becomes smaller ( $\sim 0.3$  D) when a larger 6-31+G(d, p) basis set is used. For **2** at the TD CAM-B3LYP/6-31G(d) level, the dipole moment change was found to be only  $\sim 0.1$  D. Such a small change in the ES dipole moment indicates that solvent polarity does not have a significant effect on the ES potential energy surface. This agrees well with the experimental data shown in Fig. 6.2 and Appendix Table 6.1. Fixing the B-Phe dihedral values towards  $0^\circ$  (or  $180^\circ$ ) results in a drop of  $S_1$ , a sharp rise of  $S_0$  energies and a drop in oscillator strength (from  $f = 0.3$  at optimized ES geometry to  $f = 0.0$  when B-Phe =  $20^\circ$ ). The calculations predict a very small energy barrier ( $\sim 0.5$  kcal mol $^{-1}$  relative to the optimized  $S_1$  geometry) for performing such motion. Although TD-DFT is inherently unable to adequately treat situations in which surface crossing occurs, the sudden proximity of the two surfaces accompanied by a large geometry distortion (see Fig. 6.8 c)) and drop in oscillator strength suggests that conical intersection between  $S_1$  and  $S_0$  takes place near B-Phe =  $30^\circ$  (or  $150^\circ$ ). Use of the larger 6-31+G(d,p) basis set shows a similar trend (see Appendix, Figs. 6.18 and 6.19 and discussion presented therein), which is consistent with the lack of a non-fluorescent transient intermediate in our experiments.

Although DFT calculations show reasonable agreement with the general picture obtained from our experiments, we were not able to obtain two different energy minima on the  $S_1$  surface that would account for the two different species observed in the TRIR spectra. More advanced theoretical methods would need to be employed to provide more detailed insight into the structural differences between FC and LE states.

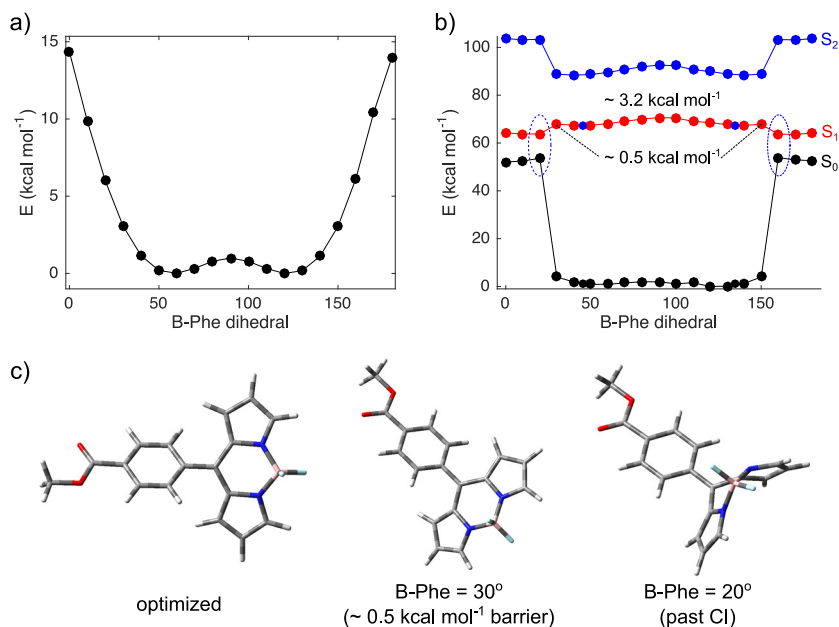


**Figure 6.8:** Partially relaxed potential energy surface scans of **1** in vacuum ((TD) CAM-B3LYP/6-31G(d)). a) Ground state optimized geometries; b) first excited state optimized geometries; conical intersections with  $S_0$  are indicated by dashed ellipses. Fully optimized  $S_1$  geometries (LE state) are indicated by blue dots on the  $S_1$  surface; c) relevant  $S_1$  geometries mentioned in the text.

## 6.4 Discussion

The experimental results can be divided into three parts. Vis-pump/vis-probe experiments provide information not only about the absorption of the potential intermediates in the visible regime, but also about the emissive species through stimulated emission. Vis-pump/mid-IR probe experiments on the other hand, provide additional structural information. Steady state fluorescence measurements offer a convenient way to quantify the factors that influence nonradiative decay of **1**, namely solvent viscosity and polarity.

The stimulated emission in vis-pump/vis-probe measurements shows three components. The first component occurs on an ultra-fast time scale and its associated time constant is less than 1.1 ps in both of the examined solvents. Fitting the individual stimulated emission time traces between 560 and 590 nm results in a gradual increase of this time constant ( $\Delta\tau \sim 0.3\text{-}0.4$  ps in both solvents), thus indicating solvation as an underlying cause for this component. This can also be observed in spectra reconstructed from global analysis of the transient-data matrices, as the DADS (Fig. 6.5 a) and c) show an increase in the relative amplitude of this component at longer wavelengths. In addition, the associated time constants show good agreement with solvation times reported for these solvents.<sup>39</sup> This con-

clusion is further consolidated by the absence of the ultra-short component in transient IR measurements and ESA in the visible region.

Subsequently, a short ps (9-12 ps) component is observed in stimulated emission and excited-state absorption. This component is also present in the case of sterically hindered BODIPY derivatives,<sup>25</sup> which shows that its contribution is not specific to unhindered BODIPY derivatives. It is therefore unlikely that this component results from interconversion between the fluorescent and the dark states (as in the case of dicyanomethylene dihydrofuran molecular rotors<sup>40</sup>). Vibrational cooling presents itself as a likely cause for this component, and has been previously proposed.<sup>25</sup> Kee and coworkers,<sup>26</sup> on the other hand, attributed this component to a structural evolution which involves nonplanar distortion of the BODIPY core in the excited state based on transient measurements in the visible region. In our vis-pump/vis-probe measurements, the ps stimulated emission decay correlates with the small rise in the excited-state absorption centered at  $\sim 430$  nm (Fig. 6.5 b) and d)). The correlation between these signals indicates 1) transformation of one species to another; and 2) relatively small change in the electronic structure, since the process does not result in drastic spectral changes. In principle, both vibrational cooling and core distortions that follow the solvation process could thus explain the picosecond component. Transient measurements in the IR, however, show a clear ps rise at  $\sim 1519$   $\text{cm}^{-1}$  (see Fig. 6.6 c)). Since we do not observe significant shifts in frequency, nor disappearance of the vibrational bands that correlates with the rise of this particular band (see Fig. 6.6 d)), this appearance of an additional vibrational transition suggests that structural relaxation of the core indeed takes place in the excited state.

The slow component ( $k_3$ ) is attributed to the decay of the fully relaxed LE state to the ground state. Since further intermediates were not observed in our measurements, excited-state decay of **1** most likely results from the surface crossing between the ground and the excited-state potential energy surfaces. TD-DFT calculations indicate that the deactivation process involves a significant change in B-Phe dihedral angle (from  $\sim 50^\circ$  to  $\sim 30\text{-}20^\circ$ ) and pucketing of the BODIPY core that follows the crossing point. This result is in partial agreement with the mechanism suggested previously, but it does not involve a dark intermediate state.<sup>26</sup> Structural deformation as large as this requires significant space, and this motion becomes strongly regulated by a combination of viscoelastic and steric characteristics of the local environment. This is evident from a high degree of correlation ( $\alpha = 0.74$ ) between the nonradiative rates and viscosity changes in glycerol. Dent and coworkers<sup>13</sup> report that fluorescence lifetimes for BODIPY rotors in non-polar castor oil and polar methanol/glycerol mixtures of equal viscosities are equal, thus showing that fluorescence deactivation of BODIPY based molecular rotors is not influenced by solvent polarity in the high viscosity regime. Fluorescence quantum yields of **1** measured in a range of aprotic solvents suggest that excited-state deactivation of **1** is governed by viscoelastic, rather than polarity effects even in the low viscosity regime (Fig. 6.2). This is consistent with TD-DFT calculations presented above, which indicate that the molecular dipole moment does not change significantly during the intramolecular movement that results in fluorescence quenching.

## 6.5 Conclusion

BODIPY-based molecular rotors are widely used viscosity sensors. In this work we have provided in-depth photo-physical and mechanistic characterization of one such molecular rotor, and used a quantitative approach to examine the influence of both viscoelastic and polarity effects of molecular environment on fluorescence deactivation of **1** by means of steady state and transient visible and IR spectroscopies with sub-picosecond temporal resolution, combined with TD-DFT calculations.

We have demonstrated that BODIPY molecular rotors are mechanistically relatively simple when compared to other types of molecular viscosity sensors, such as DCVJ (branching of the excited-state deactivation pathways<sup>41</sup>), CCVJ (presence of dark isomers<sup>42</sup>), crystal violet (multiple rotating units, prone to photoionization<sup>43</sup>) or DCDHF (solvent dependent deactivation pathway<sup>40</sup>).

The excited-state deactivation pathway of **1** is the same in non-polar toluene and polar MeCN. After initial photo-excitation solvent relaxation takes place (sub-ps). Following the solvation, structural relaxation of the BODIPY core and/or vibrational cooling takes place on a timescale of 9-12 ps. After reaching the optimal excited-state geometry, partial twisting of the phenyl group leads to a conical intersection with the ground-state potential energy surface and results in ground-state re-population. This process occurs on time scales of  $\sim 115$  and  $\sim 50$  ps for **1** in toluene and MeCN, respectively. Our data strongly suggests that viscoelastic/free volume effects have a dominant influence on excited-state deactivation of **1** both in low and high-viscosity regimes, and that solvent polarity plays a minimal role. Despite the general absence of polarity effects, the electron-withdrawing ester group does increase the rate of nonradiative decay, making **1** a BODIPY probe with a larger dynamic range than similar BODIPY derivatives reported in the literature.<sup>7,8,10-13,15,20-24,26,30</sup>

## 6.6 Appendix to Chapter 6

### 6.6.1 Determining the position of spectral maxima

As noted in the main text, Stokes shifts exhibited by **1** are very small. This makes the task of finding peak locations precisely very important. Positions of absorption and emission maxima in pure solvents and solvent mixtures were determined in the same way, which is described below.

The spectral data was obtained by measuring fluorescence counts in 1 nm steps. Due to the low fluorescence quantum yield, the data were too noisy to determine the position of spectral maximum with sufficient certainty. First, the spectra were converted to the wavenumber representation. Because such spectra are not uniformly sampled, cubic spline interpolation was used in order to obtain uniformly sampled data (which produces better fits). Since we were interested in the position of the spectral maxima, we have selected the data points which have at least 85 % of the maximal count value and used a Gaussian function to fit the peaks. A typical result of this procedure is shown in Fig. 6.9. Errors were

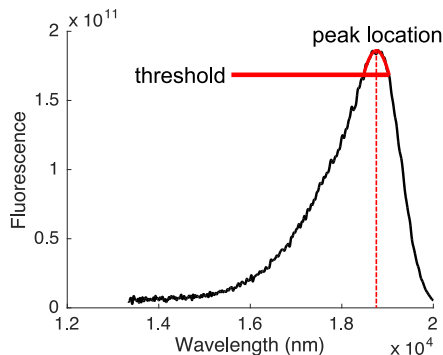


**Figure 6.9:** Representative example demonstrating the fitting procedure used in determining location of the excitation / emission maxima.

estimated from uncertainties (95 % confidence interval) of the Gaussian fit (error bars in Fig. 6.11).

## 6.6.2 Stokes shifts

Although absorption and emission spectra of **1** exhibit hypsochromic shifts, the Stokes shifts increase as a function of solvent's orientation polarization and could be quantified, as described below.

The difference between the dipole moment of the ground state and that of the excited state ( $\Delta\mu$ ) can be experimentally estimated from the Lippert-Mataga (LM) expression, where Stokes shifts are expressed as a function of the solvent's orientation polarization.<sup>44</sup> In its commonly used form, LM only considers the polarization induced in a solvent by the ground- and excited-state dipoles.<sup>31</sup> Polarizability of the solute is taken into account in the polarizable point-dipole dielectric continuum model,<sup>9,45,46</sup> in which the Stokes shift is expressed as a function of  $d_c(\epsilon) - d_c(n^2)$  defined in Eqs. 6.6 and 6.7, where  $\epsilon$  represents relative permittivity and  $n$  refractive index of the solvent. In these expressions,  $c$  is a solute polarizability parameter which can be expressed as  $c = \alpha/a^3$ , where  $\alpha$  is a solute isotropic polarizability (256 Bohr<sup>3</sup>) and  $a$  (9.77 Bohr) is the effective radius of the solute. Both parameters were obtained from DFT calculations. In the case of **1**,  $c$  is estimated to be 0.27. In order to obtain the dipole moment difference we have measured absorption and emission spectra of **1** in a series of toluene/MeCN mixtures for which the values of refractive indices<sup>47</sup> and dielectric constants<sup>48</sup> can be interpolated based on the values reported in the literature.

$$\nu_{abs} - \nu_{em} = \frac{2}{hc} [d_c(\epsilon) - d_c(n^2)] \frac{\Delta\mu_{S_1-S_0}^2}{a^3} + h\nu_{abs}^0 - h\nu_{em}^0 \quad (6.6)$$

$$d_c(x) = \frac{d_0(x)}{1 - 2cd_0(x)} = \frac{x - 1}{2(1 - c)x + (1 + 2c)} \quad (6.7)$$

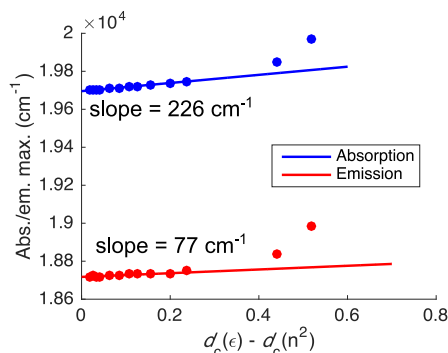


**Figure 6.10:** Measured spectral maxima plotted against the solvent polarity function  $f(\epsilon)$  in toluene/MeCN mixtures.

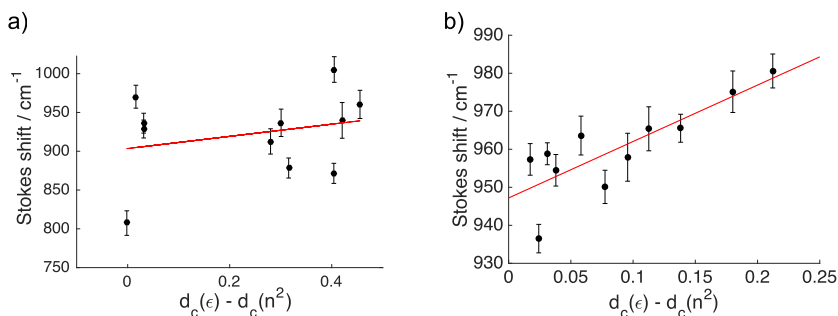


**Figure 6.11:** Stokes shifts of **1** as a function of solvent polarity. a) Pure solvents; b) toluene/MeCN mixtures.

$$d_0(x) = \frac{x - 1}{2x + 1} \quad (6.8)$$

$$\Delta\mu = \sqrt{9.9316 \times 10^{-5} \times slope \times a^3} \quad (6.9)$$

Figure 6.10 shows spectral maxima positions plotted against modified solvent's orientational polarization function ( $d_c(\epsilon) - d_c(n^2)$ ) in mixtures of toluene and MeCN (0-100 % v/v). At relatively low MeCN concentrations, the relationship between the spectral maxima and  $d_c(\epsilon) - d_c(n^2)$  is linear and therefore indicates that specific interactions do not play a significant role. As MeCN concentrations increase (>70 % by volume), deviations from the linear trend are observed. A larger point scatter can be observed in case of the emission maxima. This occurs due to the difficulties which are inherent to emission spectra measurements for fluorophores with very low fluorescence quantum yields.

Fig. 6.11 shows the Stokes shift as a function of  $d_c(\epsilon) - d_c(n^2)$  pure solvents (a) and toluene/MeCN mixtures (b) in which specific interactions can be neglected (see Fig. 6.10). The linear fit of the Stokes shift *vs* the modified orientational polarization function  $d_c(\epsilon) - d_c(n^2)$  in pure solvents produces a slope of  $85 \pm 210$

$\text{cm}^{-1}$ . The points obtained for pure solvents are very scattered, and a linear correlation between the Stokes' shifts and orientational polarization function can not be ascertained (errorbar of  $210 \text{ cm}^{-1}$  with 95% confidence level). Nonetheless, from Eq. 6.9, the slope of  $85 \text{ cm}^{-1}$ , and the effective solute radius of  $a = 5.17 \text{ \AA}$  we estimate the difference between ground- and excited-state dipole moments to be  $\Delta\mu = 1.1 \text{ D}$ . The points are significantly less scattered in toluene/MeCN mixtures, where specific interactions are small, and refractive indices/dielectric constants change systematically. An obvious correlation between the Stokes shift and the  $d_c(\epsilon) - d_c(n^2)$  parameter can be observed for these data, where we obtain a slope of  $148 \pm 79 \text{ cm}^{-1}$ . This corresponds to a dipole moment difference of  $\Delta\mu = 1.4 \pm 0.9 \text{ D}$ .

### 6.6.3 Dependence of fluorescence quantum yields on solvent polarity and viscosity

In order to check whether the solvent polarity plays a significant role in fluorescence deactivation of **1**, we measured its fluorescence quantum yields in a range of aprotic solvents. The quantum yields were determined relative to the fluorescence quantum yield of **1** in MeCN, which was measured relative to fluorescein in 0.1 M NaOH ( $\Phi_f = 0.89$ ).<sup>49</sup>

**Table 6.1:** Fluorescence data of **1** measured in different solvents.

Solvent	$\eta^a/\text{cP}$	$\epsilon_r^b$	$f(\epsilon)^c$	$\Phi_f^d/\%$	$k_{nr}^e \times 10^{-10} \text{ s}^{-1}$	$\lambda_{max,abs}^f/\text{cm}^{-1}$	$\lambda_{max,em}^g/\text{cm}^{-1}$
dioxane	1.37	2.25	0.23	1.43	0.96	19941	19000
EtOAc	0.43	6.02	0.38	0.65	2.12	19931	19014
THF	0.48	7.58	0.41	0.70	1.99	19852	18909
Acetone	0.32	20.70	0.46	0.49	2.86	19940	19000
MeCN	0.35	37.50	0.48	0.50	2.78	19977	19020
DMSO	1.99	46.70	0.48	1.11	1.25	19740	18734
DCM	0.43	8.93	0.42	0.93	1.49	19803	18927
hexane	0.30	1.88	0.18	0.72	1.93	19863	19056
toluene	0.59	2.37	0.24	0.80	1.73	19708	18741
glycerol	1412	42.50	0.48	39.72	0.02	19735	18907

<sup>a</sup> Viscosity ( $\eta$ ) obtained from ref. 50; <sup>b</sup> Values for relative permittivity ( $\epsilon_r$ ) obtained from ref. 50; <sup>c</sup> Solvent's polarity function  $f(\epsilon) = (\epsilon - 1)/(2\epsilon + 1)$ ; <sup>d</sup> Fluorescence quantum yields; fluorescein in 0.1 M NaOH ( $\Phi_f = 0.89$ )<sup>49</sup> was used as a reference; <sup>e</sup> Nonradiative rate calculated from  $\Phi_f$ ; <sup>f</sup> Absorption maximum; <sup>g</sup> Emission maximum.

### 6.6.4 Time correlated single photon counting

#### Fluorescence lifetime of **1** in PMMA

To examine fluorescence lifetime of the confined probe, we measured its fluorescence decays in strongly confining polymethyl methacrylate (PMMA) matrix. The curve was fitted by iterative convolution of three exponential functions with the measured instrument response functions. This produced fluorescence lifetimes of  $\tau_1 = 11330 \text{ ps}$  (0.2 %),  $\tau_2 = 7149 \text{ ps}$  (93.7 %), and  $\tau_3 = 915 \text{ ps}$  (6.1 %) with

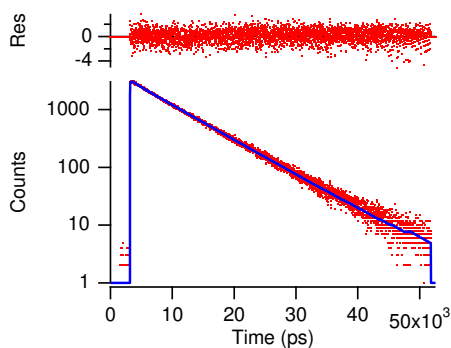


**Figure 6.12:** Fluorescence decay of **1** in PMMA.

$\chi^2 = 1.08$ . The average fluorescence lifetime (7.12 ns) was calculated according to Eq. 6.10. The fluorescence decay curve of **1** in PMMA matrix is shown in Fig. 6.12.

$$\tau_{avg} = \frac{A_1\tau_1^2 + A_2\tau_2^2 + A_3\tau_3^2}{A_1\tau_1 + A_2\tau_2 + A_3\tau_3} \quad (6.10)$$

### 6.6.5 Additional details on vis-pump/vis-probe measurements of **1**

A rise component can be observed in the vis/vis TA experiments in the ESA region. Representative curves (after filtering of the two most prominent components based on singular value decomposition in order to reduce noise) are shown in Fig. 6.13.

Stimulated emission time traces monitored at different energies indicate that solvent relaxation takes place on very short time scales. As the emission energy decreases, the rise component becomes longer and pronounced. Time traces taken at 530, 550 and 580 nm for **1** in MeCN are shown in Fig. 6.14 and look similar to the ones obtained in toluene (not shown). Single-trace fits produce time constants of 0.16, 0.42 and 0.57 ps for time traces monitored at 530, 550 and 580 nm in MeCN, respectively (time constants of the two emissive components have been fixed to 9.4 and 50 ps obtained by global analysis).

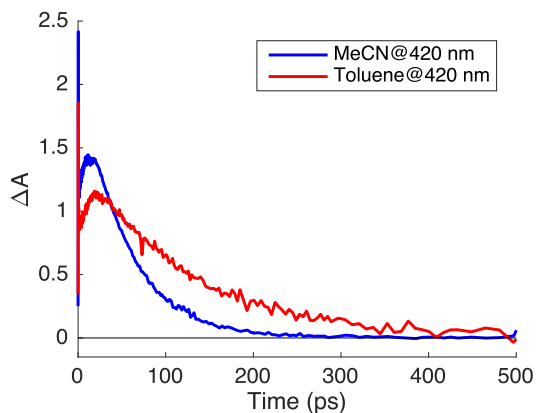


**Figure 6.13:** Excited-state absorption time traces obtained by vis-pump/vis-probe measurements for **1** in MeCN.

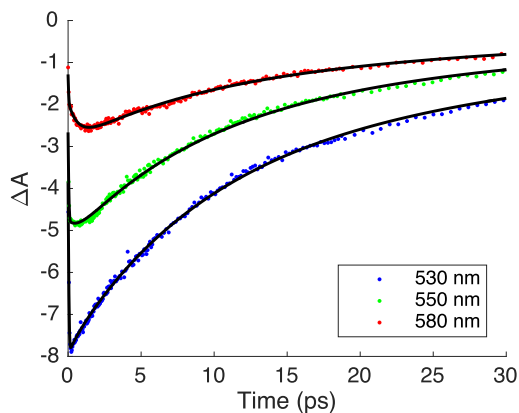


**Figure 6.14:** Stimulated emission time traces for **1** in MeCN obtained by vis-pump/vis-probe transient spectroscopy. Fits obtained by global analysis of the whole transient matrix with the sequential model are shown in black.

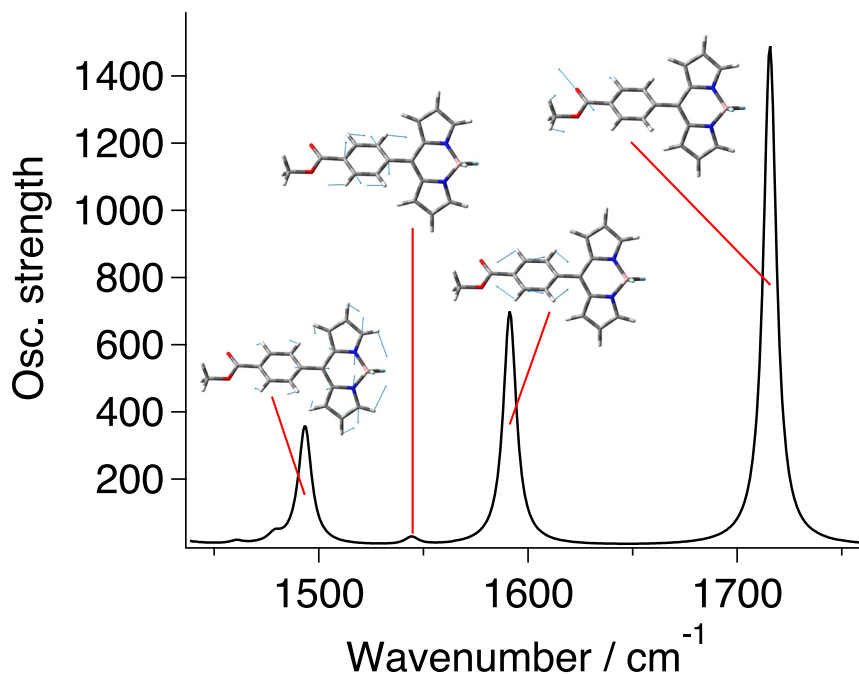


**Figure 6.15:** Assignment of the relevant vibrational modes calculated with TD-DFT CAM-B3LYP/6-31+G(d,p) level of theory in vacuum. The band located around  $1490\text{ cm}^{-1}$  consist of multiple modes involving the same atoms, and only the most intense one is shown.

### 6.6.6 Calculated vibrational spectra and mode assignment

We calculated ground- and excited-state species vibrational spectra with CAM-B3LYP/6-31G(d) and CAM-B3LYP/6-31+G(d,p) levels of theory in vacuum and with PCM<sup>29</sup> MeCN solvation. We observed modest improvement when the larger basis set was used. Vibrational spectra calculated for vacuum were more similar to the experimental spectra than those calculated with PCM solvation. The experimental and calculated spectra are compared in Fig. 6.6. Fig. 6.15 shows vibrational modes with their respective frequencies obtained with CAM-B3LYP/6-31+G(d,p) in vacuum. The region  $\sim 1520\text{ cm}^{-1}$ , where we observe a rise in ESA signal contains only modes associated with the BODIPY core, or the BODIPY core modes mixed with vibrational modes on the phenyl ring.

### 6.6.7 Excitation energies and potential energy surface scans

Excitation energies and oscillator strengths calculated with the two basis sets for **1** in vacuum are shown in Figure 6.16. The calculated excitation energies (CAM-B3LYP/6-31+G(d,p)) of **1** decrease from vacuum to MeCN (3.09 eV in vacuum; 2.89 eV in toluene; 2.68 eV in MeCN). Emission energies obtained by calculations

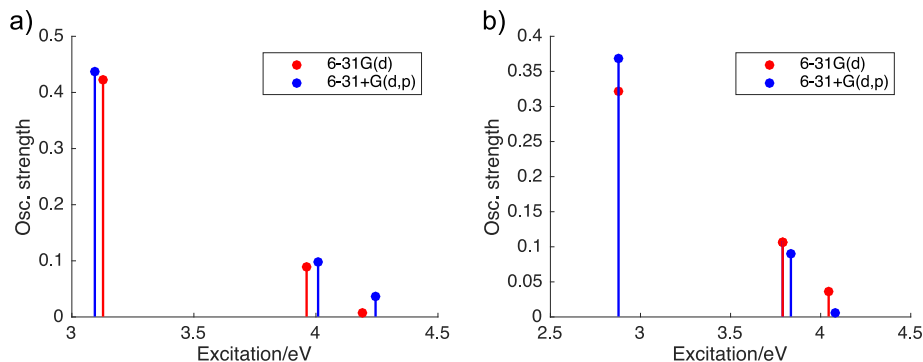


**Figure 6.16:** Comparison of the calculated excitation a) and emission b) energies *vs* oscillator strengths obtained with 6-31G(d) and 6-31+G(d,p) in vacuum.

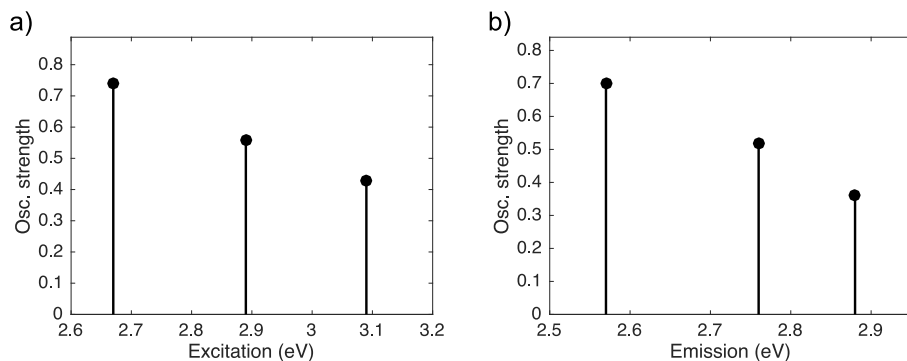


**Figure 6.17:** Comparison of the calculated excitation a) and emission b) energies *vs* oscillator strengths obtained with 6-31+G(d,p) in vacuum, toluene and MeCN.

follow the same trend (2.88 eV in vacuum; 2.76 eV in toluene; 2.58 eV in MeCN). We attribute the disagreement between the experimental (where we observe blue shift in more polar solvents) and calculated trends to limitations of the PCM model in treating non-electrostatic effects<sup>51</sup>.

The photophysical picture obtained by using partially relaxed potential energy surface scans with the larger 6-31+G(d,p) basis set is consistent with the one obtained from CAM-B3LYP/6-31G(d) (Fig. 6.18). Twisting is, as in the case of 6-31G(d) basis set accompanied by an abrupt drop in oscillator strength (from 0.34 at B-Phe = 30° to 0.0081 at B-Phe = 20°). Estimated energy barriers are 1.2 kcal mol<sup>-1</sup> (at B-Phe = 30°) and 2.3 kcal mol<sup>-1</sup> (at B-Phe = 90°). Comparison of the oscillator strengths *vs* P-Phe dihedral are shown in Fig. 6.19.

## Discussion

By comparing the 6-31G(d) and 6-31+G(d,p) results, we found that the 6-31+G(d,p) basis set provides modest improvement in the excitation energies and calculated

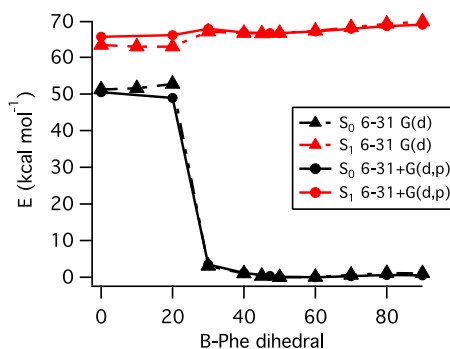


**Figure 6.18:** Comparison of the partial potential energy surface scans obtained with TD CAM-B3LYP/6-31G(d) and TD CAM-B3LYP/6-31+G(d,p) levels of theory.

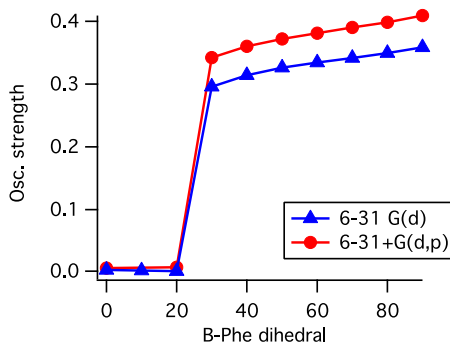


**Figure 6.19:** Oscillator strengths obtained with CAM-B3LYP/6-31G(d) and CAM-B3LYP/6-31+G(d,p) level of theory *vs* B-Phe dihedral values.

frequencies, but does not change the general trends. The optimized ground state structure (CAM-B3LYP/6-31+G(d,p)) is characterized by the planar BODIPY core (Fig. 7 a), main text) which forms a B-Phe dihedral angle of 57.7°. Including MeCN (or toluene) solvation does not influence the structure significantly in the ground state. Optimization of the first excited state in vacuum results in a slight distortion on the BODIPY core which assumes a butterfly-like shape (see Fig. 7 b). The B-Phe dihedral angle, notably, decreases from 57.7° in the ground state to 47.3° in the excited state. Including toluene (or MeCN) solvation results in a planar core geometry of the first excited state. The B-Phe dihedral of the optimized geometries in toluene changes from 57.6° in the ground state to 48.1° in the first excited state. Including MeCN solvation produces dihedrals of 56.7° and 49.9° for the ground and the first excited state, respectively.

The partial excited-state potential energy surface scan in vacuum (6-31G(d) basis set, Figure 6.8 b)) reveals the presence of four minima in the scanned range

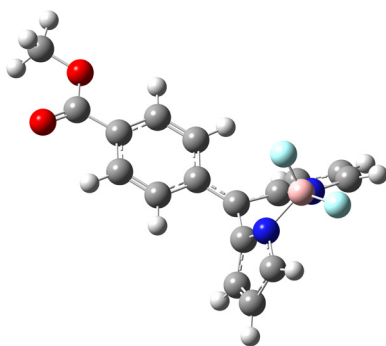


**Figure 6.20:** The structure of the apparent global minimum (B-Phe = 2 deg) reached by B-Phe dihedral twist optimized with CAM-B3LYP/6-31G(d) level of theory. The optimization with 6-31+G(d,p) does not lead to a minimum.

of 0-180°. Two of these minima could not be reproduced with the larger basis set (6-31+G(d,p)). The two minima located near the FC region correspond to the excited-state optimized geometries which are referred to as the LE state. Representative structures of the LE state are shown in Fig. 6.7 b). These structures are characterized by relatively large oscillator strength values ( $f=0.32$  at CAM-B3LYP/6-31G(d) optimized geometry). The other two structures (see Fig. 6.20), which represent global minima (but only with the smaller basis set; see below), are not expected to show fluorescence due to the low oscillator strength values ( $f=0.002$  at CAM-B3LYP/6-31G(d) optimized geometry). In addition, large structural changes in the core geometry (Fig. 6.20) take place suddenly once the dihedral values change from  $\sim 30\text{-}20^\circ$  with CAM-B3LYP level of theory (in the case of both examined basis sets). This, in combination with oscillator strength drop and general proximity of the ground and excited-state potential energy surfaces strongly suggests that surface crossing occurs near these coordinates.

As in the ground-state calculation, two LE state minima are located on the  $S_1$  surface and correspond to the two excited-state conformers. These minima are separated by a small energy barrier ( $\sim 3.2$  kcal mol $^{-1}$ ) which is somewhat greater than the barrier which separates the two conformers in the ground state. The decrease in B-Phe dihedral (or its increase towards 180°) results in  $S_1$  energy drop, which is accompanied by a rise in energy of the ground-state structure. The estimated energy barrier for this rotation is only 0.5 kcal mol $^{-1}$ , indicating that this motion occurs easily at room temperature.

Although the change in B-Phe angle towards 0° (or 180°) leads to a global minimum in the case of the 6-31G(d) basis set, geometry optimizations become increasingly difficult as dihedral angle approaches the extreme values. Change in dihedral is also accompanied by a sudden drop in oscillator strength ( $f = 0.3 \rightarrow 0.002$ , from 30° to 20°, see Fig. 6.19). Since we do not experimentally observe dark transient intermediates associated with these highly distorted minima, the presence of a

conical intersection near these coordinates is the most likely explanation for the observed fluorescence deactivation and its high efficiency.

We were not able to find the minimum that would be associated with the FC state (due to which  $\sim 10$  ps time constant is observed). The most likely reason is the overall flatness of the excited-state potential energy surface, since even increasing the grid size and varying the starting geometries did not result in stable geometries different from the one attributed to the LE state (or the distorted structure with B-Phe dihedral  $\sim 0$ ). It is likely that more advanced theoretical models would need to be used to find such geometry (if it exists), but such calculations are out of the scope of the current paper.

## References

1. Loutfy, R. O. *Macromolecules* **1981**, *14*, 270–275.
2. Loutfy, R. O.; Arnold, B. A. *J. Phys. Chem.* **1982**, *86*, 4205–4211.
3. Loutfy, R. O.; Teegarden, D. M. *Macromolecules* **1983**, *16*, 452–456.
4. Dreger, Z.; White, J.; Drickamer, H. *Chem. Phys. Lett* **1998**, *290*, 399–404.
5. Dreger, Z.; Lang, J.; Drickamer, H. *Chem. Phys.* **1992**, *166*, 193–206.
6. Zhu, D.; Haidekker, M. A.; Lee, J.-S.; Won, Y.-Y.; Lee, J. C.-M. *Macromolecules* **2007**, *40*, 7730–7732.
7. Alamiry, M. A.; Benniston, A. C.; Copley, G.; Elliott, K. J.; Harriman, A.; Stewart, B.; Zhi, Y.-G. *Chem. Mater.* **2008**, *20*, 4024–4032.
8. Levitt, J. A.; Kuimova, M. K.; Yahioğlu, G.; Chung, P.-H.; Suhling, K.; Phillips, D. *J. Phys. Chem. C* **2009**, *113*, 11634–11642.
9. Jin, H.; Liang, M.; Arzhantsev, S.; Li, X.; Maroncelli, M. *J. Phys. Chem. B* **2010**, *114*, 7565–7578.
10. Alamiry, M. A.; Bahaidarah, E.; Harriman, A.; Bura, T.; Ziesel, R. *RSC Adv.* **2012**, *2*, 9851–9859.
11. Hosny, N. A.; Mohamedi, G.; Rademeyer, P.; Owen, J.; Wu, Y.; Tang, M.-X.; Eckersley, R. J.; Stride, E.; Kuimova, M. K. *Proc. Natl. Acad. Sci. U.S.A.* **2013**, *110*, 9225–9230.
12. López-Duarte, I.; Vu, T. T.; Izquierdo, M. A.; Bull, J. A.; Kuimova, M. K. *Chem. Comm.* **2014**, *50*, 5282–5284.
13. Dent, M. R.; López-Duarte, I.; Dickson, C. J.; Geoghegan, N. D.; Cooper, J. M.; Gould, I. R.; Krams, R.; Bull, J. A.; Brooks, N. J.; Kuimova, M. K. *Phys. Chem. Chem. Phys.* **2015**, *17*, 18393–18402.
14. Suhina, T.; Weber, B.; Carpentier, C. E.; Lorincz, K.; Schall, P.; Bonn, D.; Brouwer, A. M. *Angew. Chem. Int. Ed.* **2015**, *54*, 3688–3691.
15. Hosny, N.; Fitzgerald, C.; Vyšniauskas, A.; Athanasiadis, A.; Berkemeier, T.; Uygur, N.; Pöschl, U.; Shiraiwa, M.; Kalberer, M.; Pope, F.; Kuimova, M. K. *Chem. Sci.* **2016**, *7*, 1357–1367.
16. Tang, B. Z.; Solntsev, K. M. *J. Mat. Chem. C* **2016**, *4*, 2638–2639.

17. Treibs, A.; Kreuzer, F.-H. *Justus Liebigs Ann. Chem.* **1968**, *718*, 208–223.
18. Li, F.; Yang, S. I.; Ciringh, Y.; Seth, J.; Martin, C. H.; Singh, D. L.; Kim, D.; Birge, R. R.; Bocian, D. F.; Holten, D.; Jonathan S, L. *J. Am. Chem. Soc.* **1998**, *120*, 10001–10017.
19. Förster, T.; Hoffmann, G. *Z. Phys. Chem.* **1971**, *75*, 63–76.
20. Levitt, J. A.; Chung, P.-H.; Kuimova, M. K.; Yahiolglu, G.; Wang, Y.; Qu, J.; Suhling, K. *ChemPhysChem* **2011**, *12*, 662–672.
21. Hungerford, G.; Allison, A.; McLoskey, D.; Kuimova, M. K.; Yahiolglu, G.; Suhling, K. *J. Phys. Chem. B* **2009**, *113*, 12067–12074.
22. Bahaidarah, E.; Harriman, A.; Stachelek, P.; Rihn, S.; Heyer, E.; Ziessele, R. *Photochem. Photobiol. Sci.* **2014**, *13*, 1397–1401.
23. Vyšniauskas, A.; Qurashi, M.; Gallop, N.; Balaz, M.; Anderson, H. L.; Kuimova, M. K. *Chem. Sci.* **2015**, *6*, 5773–5778.
24. Vu, T. T.; Méallet-Renault, R.; Clavier, G.; Trofimov, B. A.; Kuimova, M. K. *J. Mater. Chem. C* **2016**, *4*, 2828–2833.
25. Toebe, P.; Zhang, H.; Trieflinger, C.; Daub, J.; Glasbeek, M. *Chem. Phys. Lett.* **2003**, *368*, 66–75.
26. Kee, H. L.; Kirmaier, C.; Yu, L.; Thamyongkit, P.; Youngblood, W. J.; Calder, M. E.; Ramos, L.; Noll, B. C.; Bocian, D. F.; Scheidt, W. R.; Birge, R. R.; Lindsey, J. S.; Holten, D. *J. Phys. Chem. B* **2005**, *109*, 20433–20443.
27. Melanson, J. A.; Smithen, D. A.; Cameron, T. S.; Thompson, A. *Can. J. Chem.* **2013**, *92*, 688–694.
28. Frisch, M. J. et al. Gaussian 09 Revision D.01. Gaussian Inc. Wallingford CT 2009.
29. Tomasi, J.; Mennucci, B.; Cammi, R. *Chem. Rev.* **2005**, *105*, 2999–3094.
30. Hedley, G. J.; Ruseckas, A.; Harriman, A.; Samuel, I. D. *Angew. Chem. Int. Ed.* **2011**, *50*, 6634–6637.
31. Lakowicz, J. R. *Principles of Fluorescence Spectroscopy*; Springer Science & Business Media, 2006.
32. Dowdy, S.; Wearden, S.; Chilko, D. *Statistics for research*; John Wiley & Sons, 2011; Vol. 512.
33. Cheng, N.-S. *Ind. Eng. Chem. Res.* **2008**, *47*, 3285–3288.
34. Strickler, S.; Berg, R. A. *J. Chem. Phys.* **1962**, *37*, 814–822.
35. Yanai, T.; Tew, D. P.; Handy, N. C. *Chem. Phys. Lett.* **2004**, *393*, 51–57.
36. Dreuw, A.; Head-Gordon, M. *Chem. Rev.* **2005**, *105*, 4009–4037.
37. Zhao, Y.; Truhlar, D. G. *J. Phys. Chem. A* **2006**, *110*, 13126–13130.
38. Pedone, A. *J. Chem. Theory Comput.* **2013**, *9*, 4087–4096.
39. Horng, M.-L.; Gardecki, J.; Maroncelli, M. *J. Phys. Chem. A* **1997**, *101*, 1030–1047.
40. Suhina, T.; Amirjalayer, S.; Mennucci, B.; Woutersen, S.; Hilbers, M.;

- Bonn, D.; Brouwer, A. M. *J. Phys. Chem. Lett.* **2016**, *7*, 4285–4290.
41. Zhang, W.; Lan, Z.; Sun, Z.; Gaffney, K. J. *J. Phys. Chem. B* **2012**, *116*, 11527–11536.
42. Rumble, C.; Rich, K.; He, G.; Maroncelli, M. *J. Phys. Chem. A* **2012**, *116*, 10786–10792.
43. Bhasikuttan, A.; Sapre, A.; Rao, K.; Mittal, J. *Photochem. Photobiol.* **1995**, *62*, 245–250.
44. Mataga, N.; Kaifu, Y.; Koizumi, M. *Bull. Chem. Soc. Jpn.* **1956**, *29*, 465–470.
45. Arzhantsev, S.; Zachariasse, K. A.; Maroncelli, M. *J. Phys. Chem. A* **2006**, *110*, 3454–3470.
46. Dahl, K.; Biswas, R.; Ito, N.; Maroncelli, M. *J. Phys. Chem. B* **2005**, *109*, 1563–1585.
47. Shams, A. K. *J. Al-Nahrain Univ.* **2011**, *14*, 75–85.
48. Ritzoulis, G.; Papadopoulos, N.; Jannakoudakis, D. *J. Chem. Eng. Data* **1986**, *31*, 146–148.
49. Würth, C.; Grabolle, M.; Pauli, J.; Spieles, M.; Resch-Genger, U. *Nat. Protoc.* **2013**, *8*, 1535–1550.
50. Haynes, W. M. *CRC handbook of chemistry and physics*; CRC press, 2014.
51. Mennucci, B.; Tomasi, J.; Cammi, R.; Cheeseman, J.; Frisch, M.; Devlin, F.; Gabriel, S.; Stephens, P. *J. Phys. Chem. A* **2002**, *106*, 6102–6113.